

Contents lists available at ScienceDirect

Journal of the Mechanics and Physics of Solids

journal homepage: www.elsevier.com/locate/jmps





Physics-based discrete models for magneto-mechanical metamaterials

Gabriel Alkuino a,c, Teng Zhang b,c,*

- ^a Department of Physics, Syracuse University, Syracuse, 13244, NY, United States
- ^b Department of Mechanical and Aerospace Engineering, Syracuse University, Syracuse, 13244, NY, United States
- ^c BioInspired Syracuse: Institute for Material and Living Systems, Syracuse University, Syracuse, 13244, NY, United States

ARTICLE INFO

Dataset link: https://github.com/gsalkuin/lam mps-magneto-mechanical-2d

Keywords:
Magnetic actuation
Nonlocal interaction
Metamaterials
Lattice model
Dipole

ABSTRACT

Magneto-mechanical metamaterials are emerging smart materials whose mechanical responses can be tailored through structure architecture and magnetic interactions. The latter provides additional freedom in the material design space and leads to novel behaviors due to its nonlocal nature. The enriched functionalities open new possibilities in various applications, such as actuators, energy absorbers, and soft robots. However, the nonlinear and nonlocal coupling between elastic and magnetic forces poses a great challenge in the modeling and simulation of these systems, further hindering theory-based rational design strategies. Here, we focus on a class of magneto-mechanical metamaterials comprising elastic solids embedded with rigid permanent magnets. The clear separation between elastic and magnetic forces simplifies the design and fabrication process, yet their nonlocal interplay still allows for complex behaviors. We present a simulation framework for such magneto-mechanical metamaterials by combining a lattice spring model for the elastic solid with the dipole model for the magnetic interactions and implementing it in the LAMMPS molecular dynamics software. We demonstrate the capabilities of our framework by simulating a few representative structures, including shape-locking lattice metamaterials, a soft cellular solid with controllable buckling, and a metamaterial chain with phase-transforming behavior. For the shape-locking lattice metamaterials, we successfully capture the magnetic-actuation-driven reconfiguration and the nonlinear mechanical response of the curved lattices. For the soft cellular solid, we identify its buckling patterns under external non-uniform magnetic fields and simulate a buckling evolution process consistent with experiments. For the metamaterial chain, we include the strong long-range interactions among the embedded magnets and reproduce the controllable phase transitions in the experiments. Our work provides a simple yet versatile simulation methodology to investigate the nonlinear mechanical behaviors in the presence of strong external and internal magnetic forces, which will facilitate the design and analysis of magneto-mechanical materials. It can also be applied to other magnetically-driven smart structures, such as soft robots.

1. Introduction

Programming magneto-mechanical responses continues to be a promising strategy in the field of smart materials for various applications, where mechanics modeling and simulations play important roles in identifying the deformation mechanism and providing rational design guidance. Magnetic actuation is attractive due to its distinctive features, such as remote control capabilities,

E-mail address: tzhang48@syr.edu (T. Zhang).

https://doi.org/10.1016/j.jmps.2024.105759

^{*} Corresponding author.

fast responses, and easy manipulation. For example, it has been successfully applied for shape morphing of flat structures into 3D structures (Kim et al., 2018; Deng et al., 2020; Li et al., 2023) and creating deformation modes previously not available to conventional mechanical metamaterials to selectively tune mechanical properties for elastic (Zhang et al., 2023a,b), acoustic (Yu et al., 2018; Montgomery et al., 2021; Sim et al., 2023), and electromagnetic (Wu et al., 2022) wave manipulation. It can also be used to control buckling (Tipton et al., 2012) and facilitate transitions in multistable elastic structures (Loukaides et al., 2014; Chen et al., 2021; Yan et al., 2021; Pal and Sitti, 2023; Zhang et al., 2023a; Abbasi et al., 2024; Chen et al., 2024). In addition, the untethered actuation and permeability of biological tissues make it a suitable choice in designing miniature soft robots for biomedical applications (Hu et al., 2018; Kim and Zhao, 2022; Dong et al., 2022; Steiner et al., 2022; Gu et al., 2023; Tiryaki et al., 2023). These structures are typically made using composites of hard-ferromagnetic microparticles in a soft polymeric matrix. Extensive effort has been devoted to establishing constitutive models for magneto-rheological elastomers in general (Jolly et al., 1996; Ginder et al., 1999; Borcea and Bruno, 2001; Dorfmann and Ogden, 2003, 2004; Castañeda and Galipeau, 2011; Danas et al., 2012; Galipeau and Castañeda, 2013; Liu, 2014), and, more recently, for hard-magnetic soft materials capable of large deformations (Lu et al., 2023), ranging from pure-macroscopic approaches (Zhao et al., 2019; Garcia-Gonzalez, 2019; Stewart and Anand, 2023) to microstructurally-guided treatments (Mukherjee et al., 2020, 2021; Garcia-Gonzalez and Hossain, 2021a,b; Rambausek et al., 2022; Danas and Reis, 2024). Great attention has also been paid to developing various reduced-order modeling and simulation frameworks for plates (Yan et al., 2023), shells (Pezzulla et al., 2022), and beams (Wang et al., 2020; Sano et al., 2022; Huang et al., 2023). In most of the studies, however, the magnetic interactions within the composite have been homogenized and are not the main focus.

Magnetic interactions can also be utilized for self-assembly and emergent behaviors (Boncheva et al., 2005; Vella et al., 2014; Gu et al., 2019; Niu et al., 2019; Gu et al., 2023; Yang et al., 2023; Yang and Keten, 2023). Recently, strong magnets have been combined with mechanical structures to achieve different functionalities by harnessing the internal magnetic interactions. For instance, a magneto-mechanical metamaterial with a specific distribution of magnets can restore its shape (Galea et al., 2022). Mechanical metamaterials can be designed for energy and thermal management, tunable stiffness, negative Poisson's ratio or compressibility, among other things (Surjadi et al., 2019); magnetic interactions provide another means to architect desired properties. A unit cell made of rigid rotating squares with embedded magnets connected by elastic hinges can have multiple stable configurations, and the energy landscape can be tuned for nucleating and propagating transitions in the larger structure (Yasuda et al., 2020; Korpas et al., 2021; Zhang et al., 2023b; Jiao et al., 2024). An auxetic perforated elastic chain embedded with rigid magnets can produce controllable phase transitions and be programmed for high-strain-rate deformations (Liang et al., 2022). A circular arrangement of magnets can be used as building blocks for rotational multi-stability to tailor torsional response (Seyedkanani and Akbarzadeh, 2022). Magnetic inclusions in a soft matrix can be used to drive elastic instability and guide the post-buckling configuration (Arora et al., 2024).

A wide range of these structures are composed of elastic bodies and rigid magnets, which will be the focus of the current work. There is a clear separation between magnetic and non-magnetic domains, in that the elastic structure is non-magnetizable (i.e., the relative permeability outside the magnets is close to unity). These structures are easy to produce in a macroscopic setting and usually involve inserting or attaching magnets to conventional mechanical metamaterials. For these systems, the elastic and magnetic energies are uncoupled and the rigid magnets only transmit forces and torques to the underlying elastic structure—and vice versa—along their boundary. In contrast to magneto-rheological solids or fluids, there are fewer magnets in general and their arrangements are deliberately designed to realize targeted functions. A significant challenge in a theory-based rational design of these metamaterials is the nonlinear and nonlocal interplay between elasticity and magnetism.

A general modeling and simulation framework that accounts for both external and internal magnetic interactions will be beneficial for rapid prototyping and informing future experiments. Although it is certainly possible to solve the coupled magnetomechanical partial differential equations (PDE) (Rambausek et al., 2022), it can be costly, especially for sparsely distributed magnets in a non-magnetizable medium. This typically involves solving Maxwell's equations in the larger coordinate space to obtain the Maxwell stress tensor (Seyedkanani and Akbarzadeh, 2022; Arora et al., 2024), requiring special attention on handling mesh distortion due to large solid deformation. Because of this, in most models a point-dipole approximation for the magnet is used (Gu et al., 2019; Niu et al., 2019; Yasuda et al., 2020; Korpas et al., 2021; Liang et al., 2022; Liang and Crosby, 2022; Sano, 2022; Huang et al., 2023; Jiao et al., 2024). While dipolar interactions (Slesarenko, 2020) and a more accurate direct numerical integration scheme using Green's functions (Seyedkanani and Akbarzadeh, 2022) have been implemented in finite element (FE) software, most are not optimized for this purpose. In contrast, molecular dynamics (MD) has traditionally been used to simulate systems with long-range interactions. And for our intended applications, a conceptually-simple computational model based on particle interactions may be sufficient or more desirable than a variational or hybrid approach. To this end, we propose a simple but general simulation framework using the popular and highly versatile MD software LAMMPS (Thompson et al., 2022). Aside from LAMMPS being opensource, our model does not require modifying its source code, using only included packages that are actively maintained by the LAMMPS developers, therefore allowing seamless integration with the larger LAMMPS codebase for multiphysics coupling.

In this paper, we restrict our attention to planar structures. Aside from being easier to compute, it is still broad enough to capture interesting behaviors, as shown by numerous examples in the literature. The extension to 3D structures can follow similar ideas and will be done in future studies. In fact, modeling the magnetic interactions is easier in 3D than in 2D, as we will discuss in Section 4.2. This paper is outlined as follows. In Section 2, we introduce the computational model and its implementation in LAMMPS. In Section 3, we demonstrate the capabilities of our simulation framework through several examples, starting with an elastic beam with two interacting magnets, then lattice structures deformed via magnetic torque and gradient force, and, finally, a phase-transforming chain. In Section 4, we discuss the limitations of the simple models we use and possible improvements. Finally, we summarize and conclude our work in Section 5.

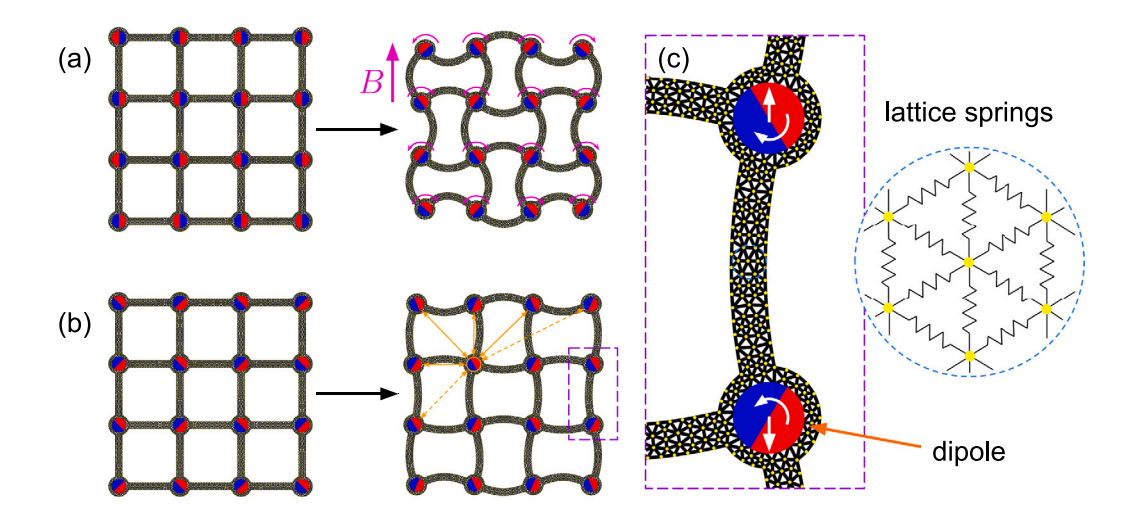


Fig. 1. Two types of magnetic interactions: (a) actuation by an external field and (b) interaction between constituent magnets. (c) Schematic of the computational model. Each magnet applies a force and torque on every other magnet. The elastic material is treated as a lattice spring system.

2. Methods

Our computational model treats the elastic material as a lattice spring system and the rigid magnets as point-dipoles, as shown in Fig. 1(c). Lattice nodes on the boundary of a magnet are rigidly 'bonded' to it to couple the force and torque between the elastic structure and the magnet. We provide more details below.

2.1. Lattice spring model

Lattice spring models (LSM) are popular in computer graphics and solid mechanics due to their speed and simplicity (Terzopoulos et al., 1987; Ostoja-Starzewski, 2002). Although not as accurate as geometrically nonlinear FEM models, they perform better than linear-elastic models for large rotations and deformation (Lloyd et al., 2007). For a regular triangular lattice in 2D, the discrete stretching energy for an isotropic, linear elastic material can be written as (Seung and Nelson, 1988)

$$U_{\text{stretch}} = \sum_{\text{bonds}} \frac{\sqrt{3}}{4} Y h \left(r - r_0 \right)^2, \tag{1}$$

where Y is Young's modulus, h is the thickness, and r and r_0 are the current and rest bond lengths, respectively. We do not consider out-of-plane bending in this paper. For an irregular lattice, this is only approximate and a more accurate model can be made by scaling the stiffness with the area of the cells adjacent to the bond (Leembruggen et al., 2023; Lloyd et al., 2007). Thus, given a triangular mesh we can turn it into an equivalent lattice spring system.

2.2. Magnetic interactions

The magnetic forces and torques can be grouped into those caused by external and internal sources. The applied external magnetic field contains all the information from the external sources. For interaction between constituent magnets, we evaluate the forces and torques directly using the dipole model. Under an external magnetic field \mathbf{B} , a magnetic point-dipole \mathbf{m} experiences a force $\mathbf{f} = \nabla(\mathbf{m} \cdot \mathbf{B})$ and torque $\mathbf{t} = \mathbf{m} \times \mathbf{B}$. A magnet can be treated as a collection of dipole elements $d\mathbf{m}(\mathbf{x}) = \mathbf{M}(\mathbf{x})dV$, where \mathbf{M} is the magnetization field. If the magnetic field is due to another dipole, we get the following well-known formulas. Given two dipoles \mathbf{m}_i and \mathbf{m}_i , the magnetic energy $U = -\mathbf{m}_i \cdot \mathbf{B}_i = -\mathbf{m}_i \cdot \mathbf{B}_i$ is

$$U = \frac{\mu_0}{4\pi r^3} \left[(\mathbf{m}_i \cdot \mathbf{m}_j) - 3(\mathbf{m}_i \cdot \hat{\mathbf{r}})(\mathbf{m}_j \cdot \hat{\mathbf{r}}) \right], \tag{2}$$

where $\mathbf{r} = \mathbf{x}_i - \mathbf{x}_i$ and $\hat{\mathbf{r}} = \mathbf{r}/r$. Therefore, the force on \mathbf{m}_i is

$$\mathbf{f}_{ij} = \frac{3\mu_0}{4\pi r^4} \left[(\mathbf{m}_i \cdot \mathbf{m}_j) \hat{\mathbf{r}} + (\mathbf{m}_i \cdot \hat{\mathbf{r}}) \mathbf{m}_j + (\mathbf{m}_j \cdot \hat{\mathbf{r}}) \mathbf{m}_i - 5(\mathbf{m}_i \cdot \hat{\mathbf{r}}) (\mathbf{m}_j \cdot \hat{\mathbf{r}}) \hat{\mathbf{r}} \right],\tag{3}$$

and the torque is

$$\mathbf{t}_{ij} = \frac{\mu_0}{4\pi r^3} \left[3(\mathbf{m}_j \cdot \hat{\mathbf{r}})(\mathbf{m}_i \times \hat{\mathbf{r}}) - \mathbf{m}_i \times \mathbf{m}_j \right]. \tag{4}$$

Here we are assuming that the magnets are 'hard', i.e., they cannot be demagnetized by an external field.

2.3. Implementation

We implement our computational model in the LAMMPS MD simulator (Thompson et al., 2022), however the following discussion should be applicable to most MD software. The elastic material treated as a lattice spring system can be imagined as a large *molecule*, where the mass nodes are *atoms* and the mesh edges are harmonic springs. The formulas for the dipole–dipole interaction are already implemented in most common MD software, albeit for electric dipoles, which can be easily repurposed for magnetic dipoles by a multiplicative factor involving the speed of light ($c^{-2} = \mu_0 \epsilon_0$). Decades of work have been put into developing fast electrostatic algorithms; a recent review is provided in George et al. (2022). They are complicated to code from scratch, which is all the more reason to use a robust and popular MD software like LAMMPS. Although most of these fast-solvers are readily available in LAMMPS, they were designed for a different purpose, primarily for chemical simulations. Our current systems of interest are planar and non-periodic, which makes FFT-based approaches inapplicable. Since we are only dealing with a sparse collection of dipoles (around 1% of the atoms), a direct evaluation is sufficient. An external magnetic field can be added using the fix efield command, with a similar change in units. Note that as of the latest stable release of LAMMPS (2 August 2023) this command only computes the torque on dipoles, so it is valid only for spatially uniform external fields. However, non-uniform fields can also be approximated by introducing physical dipoles, as we will show in Section 3.3.

The models were chosen primarily because they are easy to implement. In LAMMPS, the bond coefficients and dipole moments only need to be computed once when preparing the data file. More complicated elastic and magnetic models may require different packages or custom implementation. For handling rigid bodies, we use the RIGID package in LAMMPS. A magnet is treated as a rigid group of atoms, with the total dipole moment assigned to the atom closest to the centroid. All the atoms in a rigid group are point masses, except for the dipole that needs to be a sphere to enable rotation, whose diameter we set to the shortest bond length such that it does not significantly affect the computation of the moment of inertia. Assuming a uniform density, each mesh element has its mass split evenly among its three nodes; a more accurate method would be to account for the moments (Deussen et al., 1995). The examples presented in this paper deal with equilibrium configurations and do not include gravity, so the accurate assignment of mass and moment of inertia is not paramount. In fact, we scaled up the densities to speed up some simulations. We use the dipole atom style in LAMMPS, but a similar functionality may be achieved using the MSPIN package (Mahmood and Yingling, 2022). To model contact, we define boundary atoms and promote them to spheres, where the diameter of each atom is set to the longer of the two incident boundary edges. We use the GRANULAR package for the interaction.

There are three ways for atoms to interact. The first one is through bonds and rigid constraints. The communication is typically handled automatically by LAMMPS. In principle, the communication cutoff distance should be at least the maximum bond length expected throughout the simulation or the size of the rigid body. The second is through contact between (non-bonded) boundary atoms. A sufficient cutoff using a granular contact model is about the size of the particles. The third is the long-range magnetic dipole—dipole interactions, where a direct evaluation requires a much larger cutoff. To improve efficiency, we define a separate collection for each type of interaction using the neighbor multi command in LAMMPS (in 't Veld et al., 2008; Shire et al., 2020; Monti et al., 2022).

All geometric structures in the following examples were drawn and meshed using Gmsh (Geuzaine and Remacle, 2009), and loaded into Python using meshio (Schlömer et al., 2018). A custom Python package was written to prepare the LAMMPS data file, with the help of libigl (Jacobson et al., 2018) to handle some mesh-based calculations. Simulation output are visualized using OVITO (Stukowski, 2010).

3. Examples

In this section, we demonstrate the capability of our simulation framework through several representative examples. We will first examine the competing effects of magnetic and elastic forces in determining the stable configurations of an elastic beam with magnets on both ends. Next, we will investigate the deformation and mechanical properties of beam lattice metamaterials embedded with weak magnets, where the deformations are primarily driven by torques due to the external magnetic field. Then, we will explore another kind of magneto-mechanical structure, where the deformation is driven by the magnetic gradient force. Lastly, we will study the nonlinear mechanical behavior of a metamaterial chain with strong magnets and demonstrate the phase transformation that occurs during mechanical loading.

3.1. Investigating the stability of an elastic beam with two magnets

We first consider a very simple magneto-mechanical structure—an elastic beam with magnets on the two ends. This can be a basic building block for more complex magneto-mechanical lattice structures and may also be useful to aid in the design of self-folding soft-robotic chains composed of rigid segments with elastic joints, similar to those introduced in Gu et al. (2023) for minimally invasive surgery.

As shown in Fig. 2(a), a thin elastic beam is connected with a magnet on each end. Each magnet has a dipole moment of 785 erg/G, which can be imagined as a NdFeB (magnetization $M = 10^6$ A/m) sphere of diameter 1 cm inside a hard cube of length

¹ For circular magnets, it is also possible to replace the rigid collection with one particle. However, unlike fix nve/sphere, fix rigid does not have a disc keyword, which means spherical particles will still be treated as spheres instead of disks in 2D. A quick fix is to modify the constant SINERTIA from 2/5 to 1/2 in src/RIGID/rigid_const.h.

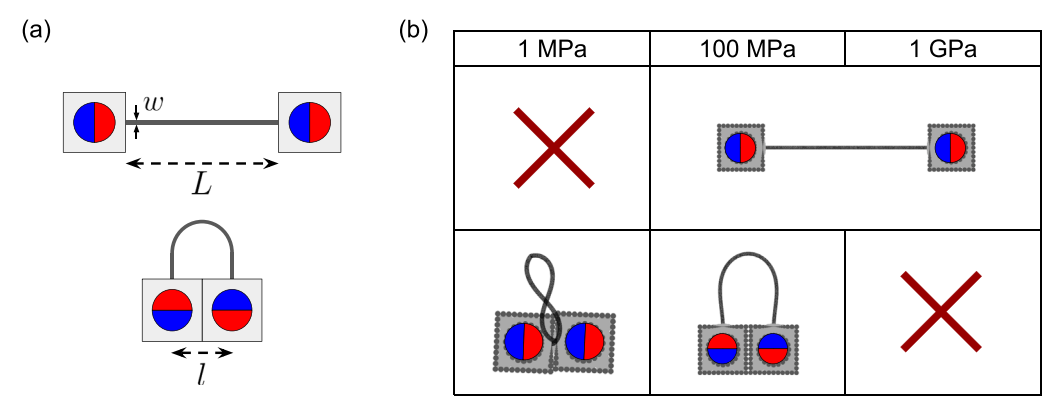


Fig. 2. (a) Schematic of a beam with two magnets showing the straight and fully folded configurations. (b) Possible stable configurations for different beam stiffness. For 1 MPa, the beam will collapse on its own.

1.5 cm. The cubes are connected by an elastic beam of length L=5.75 cm, slenderness ratio w/L=0.02, and depth (thickness) h=1.5 cm. The beam initially separates the two magnets far enough so that the self-interaction of the magnets is weak, making the straight configuration stable. If we bend the beam in the configuration shown in Fig. 2(a), the anti-parallel magnets will attract each other. We are interested in which beam stiffness can support stable straight and folded states. If the beam is too stiff, it will always revert to the straight configuration. Too soft, it may collapse under a small perturbation. This is not easy to determine analytically since the force and torque depend on the current position and orientation of the beam ends.

To test the stability of the states, we first conduct indentation tests of the beam. Starting with a straight beam, we introduce a cylindrical indenter from below that we gradually move upwards; a horizontal wall is also added to prevent the rigid ends from simply being lifted. By controlling the indentation distance, we can bend the beam at various degrees. We then release the external constraints and relax the system to its equilibrium configuration. Fig. 2(b) shows the possible stable configurations from trying to fold the beam. We numerically find that a modulus in the order of 10 - 100 MPa is stable for the straight and folded states. At 100 MPa, a beam in the folded state will become straight when a small gap (2 mm) is introduced. At 1 GPa, the beam will always want to be straight. At 1 MPa, a straight beam collapses on its own due to strong magnetic interaction and weak elastic energy (supplementary video 1).

It is interesting to note that the beam with modulus 100 MPa shows bistable configurations. To get a more quantitative analysis of the transition path, we constrain the magnets in the folded state to only allow horizontal translation, as shown in Fig. 3(a). It should be noted that without the constraint the magnets can rotate, decreasing the elastic energy and increasing the strength of the magnetic interaction, which complicates the energy landscape. This simplification of the motion enables us to compare the total energy of the system as a function of the separation distance. We numerically find a local energy maximum at a gap of 0.76 cm, beyond which the magnets will want to separate (Fig. 3(b) and (c)). The energy decreases as the gap decreases from the local maximum until the two blocks are in contact, leading to a local minimum state.

Under this constrained deformation space, we can explore the stability of the folded state by examining the force. Considering the right magnet in the folded state, the force along the *x*-direction can be expressed as

$$F_{\text{folded}} = F_{\text{elastic}} + F_{\text{magnetic}} = \alpha K / l - \frac{3\mu_0 m^2}{4\pi l^4},\tag{5}$$

where K = EI/L is the bending stiffness, $I = w^3 h/12$ is the area moment of inertia, and α is a dimensionless pre-factor we obtain from numerical simulations. Here we assume the bending deformation dominates the elastic energy and the shape of the beam is only determined by the given displacement boundary conditions and does not depend on the bending stiffness, such that α is constant. This analysis gives us $\alpha = 4.5 \times 10^7$ and a critical modulus of 360 MPa. We test this prediction by performing multiple folding test simulations (as in Fig. 3) using various moduli and find the critical modulus to be between 363 and 364 MPa.

It is fascinating to numerically observe rich and complex behaviors even in this simple setup. This demonstrates the power of harnessing nonlinear magnetic interactions in tailoring the mechanical response. We also hope our simulations can spark interest from experimentalists to test our findings. The modeling can be further improved as well. For example, the pre-factor α depends on the beam geometry and the magnet shape, requiring more simulations to get a deeper understanding. A reduced beam model will be more suitable to explore the stability phase diagram of more general setups. More advanced techniques, such as nudged elastic band methods (Wan et al., 2024), should be utilized to search for minimum energy transition paths without wall constraints in the future.

3.2. Shape-locking lattice metamaterials with weak magnets

Most actuated magneto-mechanical materials cannot maintain their shape once the external field is removed. One strategy is to utilize shape memory materials to lock the shape after magnetic actuation, which provides a new means to fabricate structures

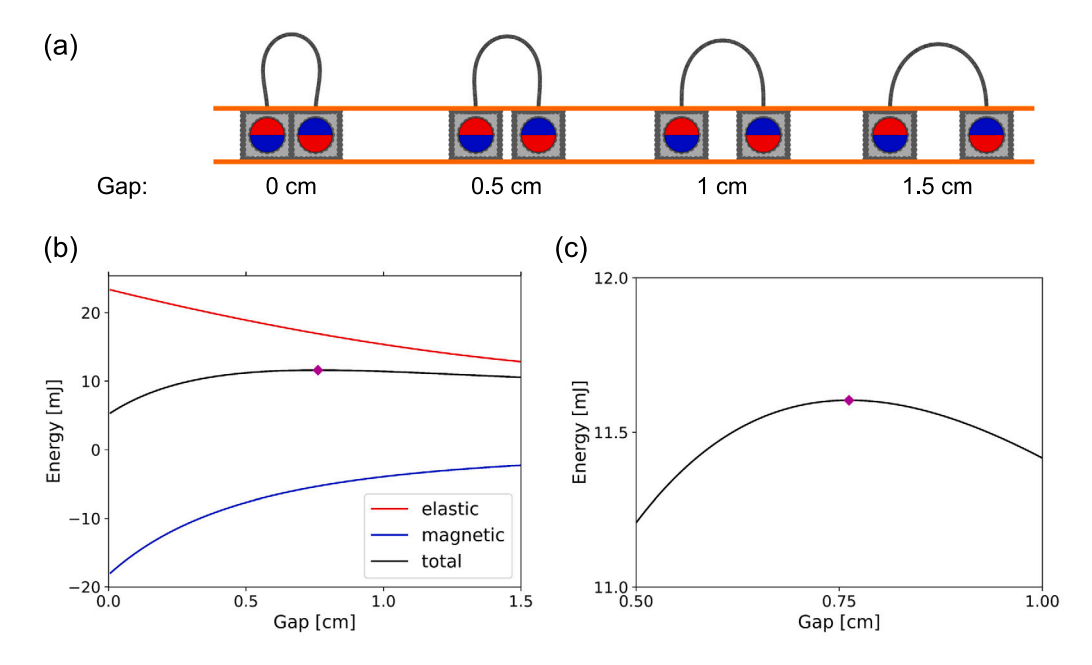


Fig. 3. (a) Unfolding the beam by horizontally pulling the magnets apart. (b) Energy diagram for a 100 MPa beam as a function of the gap distance. (c) A close-up view showing a local energy maximum.

with complex shapes (Ze et al., 2020) and microstructures (Zou et al., 2023). For example, Zou et al. (2023) used shape-memory polymers (SMP) to create shape-locking magneto-thermomechanical reprogrammable metamaterials by heating the SMP to decrease its stiffness to a value where large deformations are possible within typical actuation field strengths and cooling to increase its stiffness and lock the current shape. In one of their experiments, they deformed a square lattice using various magnetic field strengths to obtain different curved lattices and then tested their mechanical properties.

Here, we show that our discrete model can easily account for the shape memory effect and capture the changes of the stress–strain curves of the different curved lattices. Following the experiments of Zou et al. (2023), we adopt a two-stage simulation procedure with magnetic actuation followed by shape locking and mechanical loading. We first validate the magnetically-driven deformation at low stiffness by comparing our simulations with their experimental data. In Fig. 4(c), we select a few representative structures in Zou et al. (2023) to simulate their deformed configuration under a uniform external magnetic field. The exact beam dimensions used in each experimental image were not provided, except for the length which can be estimated to be 1 cm from the scale bars; nevertheless we only use them as reference shapes.

In our simulations, we set both the width and thickness to 1.5 mm. For the square structure, the beam (excluding the magnets and their case) has length L=9.75 mm (shown in Fig. 4), while for the triangular structure $L\approx 10$ –10.5 mm. From the reported values, Young's modulus was set to 3 MPa and the dipole moment was calculated by assuming a uniform magnetization M=945 kA/m in a box magnet of dimensions $3\times2\times1$ mm³. The external magnetic field was set to B=80 mT, which was the maximum strength used in their experiments. Since the field is uniform, there is no magnetic force, and the torque on a magnet will be equivalent to its point-dipole limit. Fig. 4(a) shows the initial configuration of the system. By gradually applying the external magnetic field at a particular direction (magenta arrows), we obtain (Fig. 4(b)) deformation modes in good agreement with the experiments (Fig. 4(c)). The agreement is better with the square lattice structures (first two columns) than with the triangular lattice structures (last two columns), and the accuracy for both may be further improved by tuning the dimensions of the beam.

With this validated model, we next investigate the mechanical response of the shape-locked lattices. As shown in Fig. 5(a), after deforming the lattice with an external magnetic field, we lock the shape and perform subsequent mechanical loading. The curviness of the lattice is controlled by the strength of the magnetic field. To lock the shape, we use the coordinates of the final configuration from the first stage to recalculate the rest bond lengths and increase the bond stiffness according to the modulus 2.4 GPa based on the reported value in Zou et al. (2023). An example compression test simulation is shown in Fig. 5(b) and (c) and supplementary video 2. Here, the rotation of the magnets are 0° , 6.9° , 13.5° , 25.2° corresponding to B = 0, 20, 40, 80 mT. The top and bottom walls were modeled as a row of atoms interacting with the lattice spring atoms through a repulsive soft potential. Some slipping can be observed due to the crude wall model, leading to jumps in some of the stress–strain curves. The nominal strain was calculated using the area defined by multiplying the center-to-center distance between end magnets with the thickness. The overall trend is consistent with the experiments; a curvier lattice has a lower effective modulus and delays the onset of global buckling.

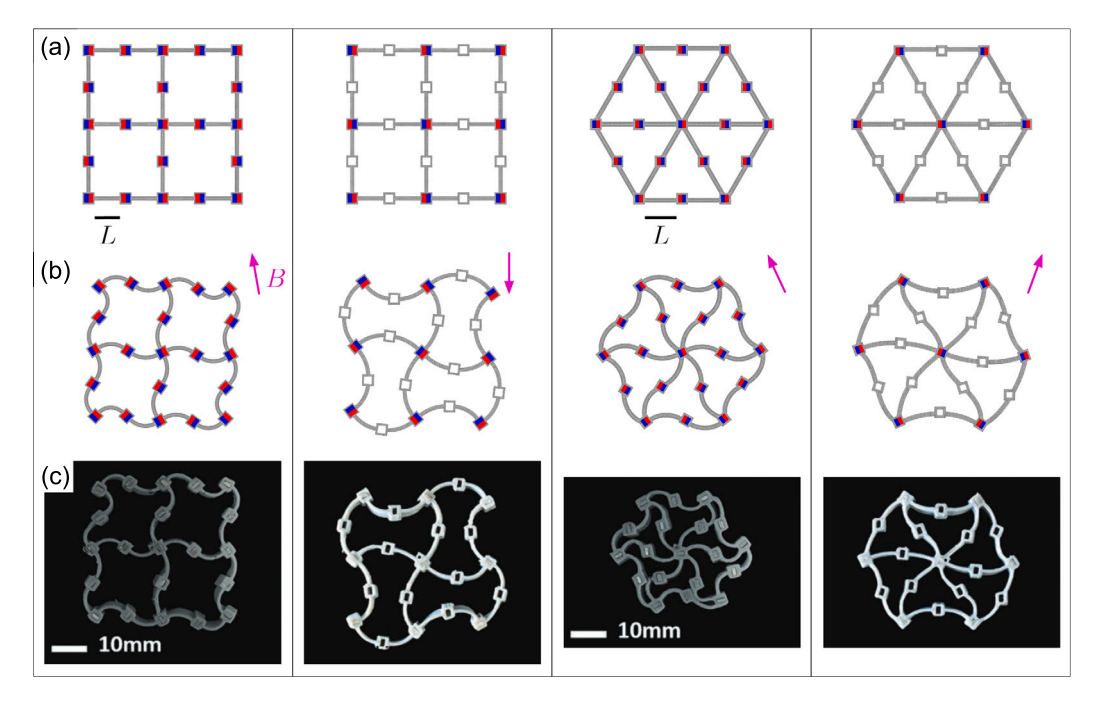


Fig. 4. Magnetically actuated chiral and achiral lattice structures. Simulation snapshots showing the (a) initial and (b) deformed configurations compared to the (c) experimental images in Zou et al. (2023).

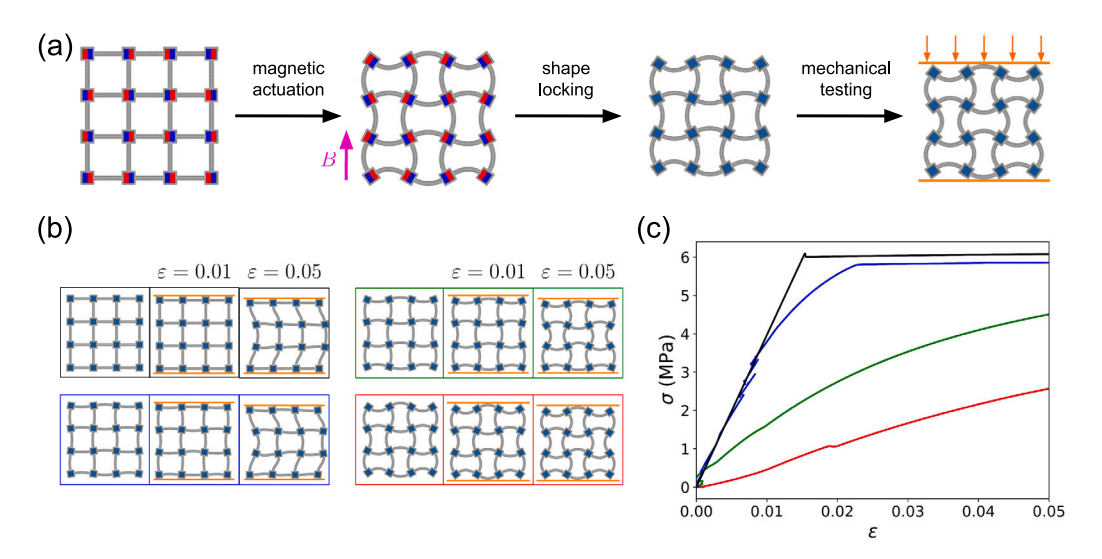


Fig. 5. (a) Schematic of the simulation protocol in Section 3.2. (b) Snapshots of the compression test showing the deformation of various lattice shapes at different strains and (c) the corresponding stress-strain curves. Here, no magnetic interactions are considered.

3.3. Buckling of a magneto-elastic solid under a non-uniform magnetic field

The examples in Section 3.2 demonstrate actuation using a uniform magnetic field, where the torque on the magnets drives the deformation. Our framework also makes it possible to study systems with deformation due to a magnetic field gradient. For the next example, we simulate the magneto-elastic buckling of a soft cellular solid with embedded magnets caused by a radial compressive force due to the magnetic gradient (Tipton et al., 2012). The experimental setup is schematically shown in Fig. 6, where the structure has 9 magnetic cylinders embedded in a thick elastomer of modulus 1.4 MPa with large circular holes. Each magnetic cylinder was made by vertically stacking five smaller axially-magnetized cylindrical magnets with moment $m = 0.014 \,\mathrm{Am^2}$. An electromagnet was placed below the structure such that the magnetic field has cylindrical symmetry. The structure can buckle and unbuckle depending on the current (Tipton et al., 2012). The full specification of the electromagnet was not provided; however, they measured the force

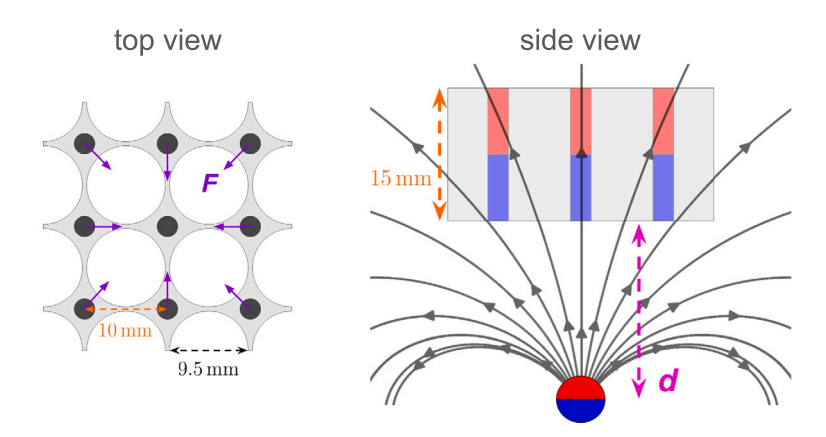


Fig. 6. Schematic of the cellular buckling simulation. The actuating electromagnet is approximated as an out-of-plane physical dipole placed below the center of the cellular structure. The magnetic field lines of the actuating dipole are shown and their gradient causes a radial compressive force.

Source: The figure is adapted from Tipton et al. (2012).

per unit current on the smaller magnet at two locations, corresponding to the bottom corner (a radial distance $\rho = 10$ mm from the center) and bottom edge ($\rho = 14.14$ mm).

We build a model to simulate the process, where we mimic the electromagnet with a strong dipole and tune its position and moment to match the compressive radial force at the two locations described above. Since the dipole moment of an electromagnetic coil is directly proportional to the current, we can establish a mapping between the dipole strength and current. Both the dipole moment and position are fitting parameters in our simulation. In cylindrical coordinates, the magnetic field of a dipole $\mu = \mu \hat{z}$ at the origin is

$$\mathbf{B} = \frac{\mu_0 \mu}{4\pi} \frac{3\rho z \hat{\rho} + (3z^2 - \rho^2) \hat{\mathbf{z}}}{(\rho^2 + z^2)^{5/2}},\tag{6}$$

and each embedded magnet will experience a force

$$F = (\mathbf{m} \cdot \nabla) \, \mathbf{B} = m \frac{\partial}{\partial \tau} \, \mathbf{B} \tag{7}$$

$$= \frac{\mu_0 m \mu}{4\pi} \left[\frac{3\rho \left(\rho^2 - 4z^2\right)}{\left(\rho^2 + z^2\right)^{7/2}} \hat{\rho} + \frac{3z \left(3\rho^2 - 2z^2\right)}{\left(\rho^2 + z^2\right)^{7/2}} \hat{z} \right]. \tag{8}$$

At a distance d=15 mm below the structure, the magnetic force will have a negative radial component and a relatively weak axial component throughout the structure. Therefore, we fix this distance and vary the dipole moment to match the forces at the two locations measured in the experiments Tipton et al. (2012). Using the linear relationship between the dipole moment and the current, we derive $m/I=0.292\,\mathrm{m}^2$. Following the experimental setup, We also fix the central magnet so that it cannot translate or rotate. We perform a buckling simulation by a repeated cycle of increasing the current by 0.1 A and letting the system relax. Without considering the interactions between embedded magnets, we determine the critical current to be 2.5 A, above which the structure will quickly buckle (Fig. 7 and supplementary video 3). This is lower than the experimental value of 3.85 A. When we decrease the current while the structure is in the fully collapsed state, it will start to unbuckle at around 1.7 A (Fig. 7 and supplementary video 3), which is lower than the experimental value of 2.9 A. The lower values of the critical currents in the simulations can be attributed to the 2D simplification of the 3D structure. The magnetic field decays from the bottom to the top surface of the solid, and this inhomogeneity (as evident from the experimental buckled shape) can be hard to capture with a planar model. In addition, the embedded magnets will exert repulsive forces on each other, further delaying the buckling. Both factors require 3D simulations, as we will discuss in Section 4.2, and will be explored in future studies.

3.4. Phase-transforming metamaterial chain with strong magnets

As a final example, we simulate the metamaterial chain shown to exhibit a solid–solid phase transition (Liang et al., 2022). Fig. 8(a) shows a sketch of 2 unit cells of the chain. Based on the reported measurements of Liang et al. (2022) the unit-cell length is L=6 mm, the magnets' diameter is 3.10 mm, the thickness of both the elastomer and the magnets is 3.18 mm, and the Young's modulus is 1.68 MPa. As shown in Fig. 8(b), an orientation parameter $Q=\cos\theta_{\uparrow}\cos\theta_{\downarrow}$ is defined to characterize different magnet configurations (Liang et al., 2022). Note that Q is invariant under the transformations $\theta_{\uparrow} \rightarrow -\theta_{\uparrow}$, $\theta_{\downarrow} \rightarrow -\theta_{\downarrow}$, $\theta_{\uparrow} \leftrightarrow \theta_{\downarrow}$, so there are plenty of ways to obtain the same Q value. We found that some configurations with the same Q value relaxed to different rest lengths, probably caused by the difference in torques (Eq. (4)). To prevent the chain from collapsing on itself under the strong magnetic attraction, each atom on the boundary of the elastomer was modeled as a granular particle; this is illustrated in Fig. 8(c).

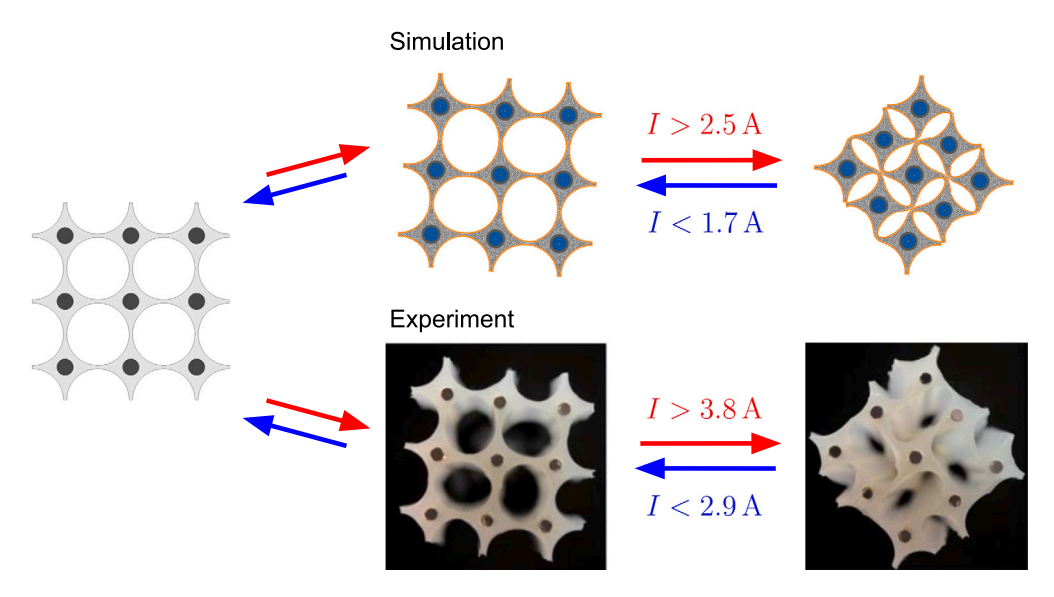


Fig. 7. The buckling and unbuckling simulation compared to the experiment. The two snapshots show the shape immediately before and after buckling. Experimental images were taken from Tipton et al. (2012). The circular holes become elliptical as the solid rotates before fully collapsing. Red/blue arrows indicate whether the current is increased/decreased to transition between two states, where the transition only occurs if the current reaches the critical value. In the experimental buckled image, the effect of the inhomogeneity in the magnetic field can be seen: the edges of the holes are in contact on the bottom surface.

For a roughly-uniform mesh, this sufficiently prevents penetration. The full chain structure used in the simulations is shown in Fig. 8(d).

We present the simulation results of a tensile test for the geometry (w = 0.13L, a = 0.17b) in Fig. 9. Our simulations successfully capture the experimentally observed phase transition for Q = 1 (Fig. 9(a) and supplementary video 2), where the three snapshots correspond to the magenta markers in Fig. 9(b), which shows the simulated stress–strain curves for various Q. This is overall consistent with the experiments (Fig. S3(a) in Liang et al., 2022). For Q = 1, the stress in the dual phase plateaus at around 15 kPa, close to the experimental value of around 12.5 kPa. A phase transition was also observed for Q = 0.5, similar to the experiments, although the simulated stress is lower than the experimental value during the phase-transition stage. For large strains, the obtained stresses were higher than what was reported in the experiments ($\sigma \approx 90$ kPa at $\varepsilon = 0.4$), which may be attributed to the limitations of the simple harmonic spring model and the assumption that the magnets remain rigidly bonded to the holes. In reality, for large strains, a small gap forms above and below the magnet as the hole deforms with the elastomer.

We can also test the effect of the dipole cutoff distance on the simulations. For example, we plot the stress–strain curve for Q=1 using different cutoff distances in Fig. 10(b). We observe for this particular system that the difference between $r_{\rm cut}=2$ cm and $r_{\rm cut}=4$ cm is marginal, and the succeeding barely noticeable, due to the rapid decay of the magnetic energy ($\sim 1/r^3$). Our numerically-identified critical cutoff value is also consistent with the force–displacement curve in Liang et al. (2022). We did not observe any difference in the simulation speed. As discussed in Section 2.3, since the dipoles have their separate neighbor list and there are only 40 of them, a shorter cutoff only shaves off a few atoms.

4. Discussion

While the simple elastic and magnetic models have demonstrated a good capability in capturing the emerging nonlinear behaviors of a wide range of magneto-mechanical metamaterials, there remain opportunities for further improvement and exploration. For better quantitative agreement, more refined models may need to be employed. With the current point-dipole model for permanent magnets, there are two limitations we discuss below. The first involves the accuracy of the dipole approximation, the second deals with the simplifications of representing a 3D system with its 2D cross section. We will further discuss potential strategies to overcome these limitations.

4.1. Improving the point-dipole approximation

It is well-known that the dipole approximation can lead to large errors for commonly used magnet shapes such as cylinders or boxes, especially when the magnets are close to each other. Although exact analytic solutions exist for the fields (Callaghan, 1960; Camacho and Sosa, 2013; Caciagli et al., 2018; Masiero and Sinibaldi, 2023), each shape will require a custom implementation (e.g., some special functions or elliptic integrals) that cannot easily be reused. In Masiero and Sinibaldi (2023), they derived an exact solution for the force and torque between coaxial cylinders. However, for more general configurations numerical integration is required; this was done in Li et al. (2018). The dipole model may be improved by treating a magnet as a collection of smaller

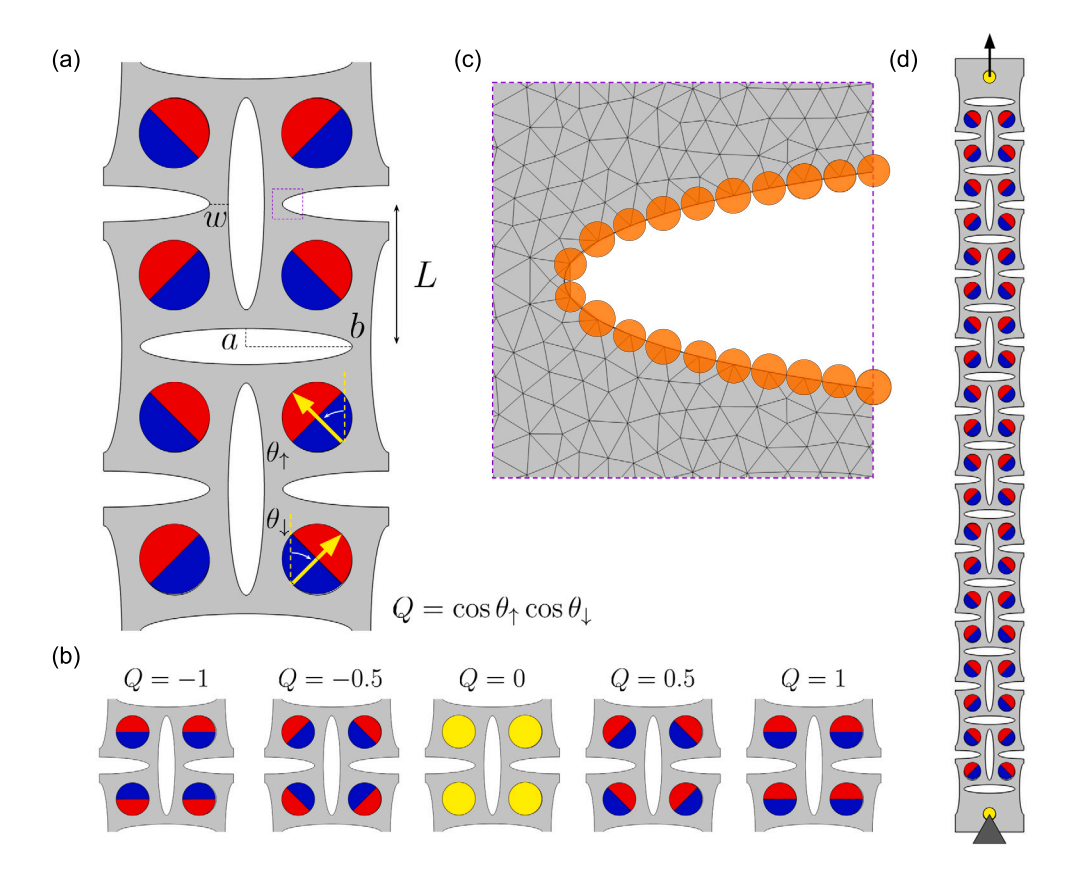


Fig. 8. The phase-transforming metamaterial chain Liang et al. (2022). (a) Sketch illustrating the geometric parameters of the elastomer chain and the orientation parameter of the magnets. (b) Different magnet arrangements and their corresponding orientation parameter used in the simulations in Fig. 9. (c) Boundary nodes are treated as granular instead of point masses to model contact. Boundary nodes are treated as granular particles. (d) Setup for the tensile test.

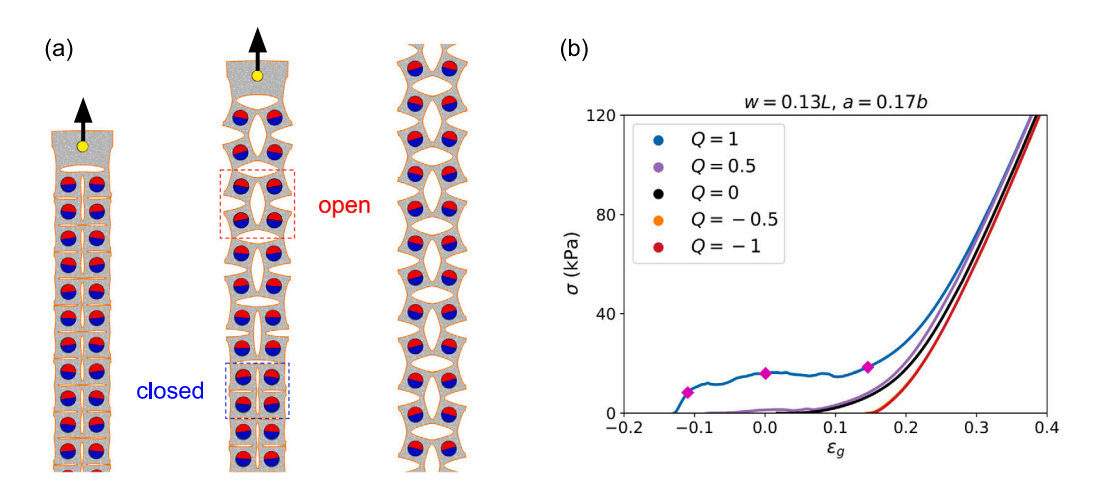


Fig. 9. Tensile test for the geometry (w = 0.13L, a = 0.17b) with different orientation parameter Q. (a) Snapshots of the Q = 1 case showing closed, dual, and open phases during loading; they occur at the magenta points in (b) the stress–strain curves.

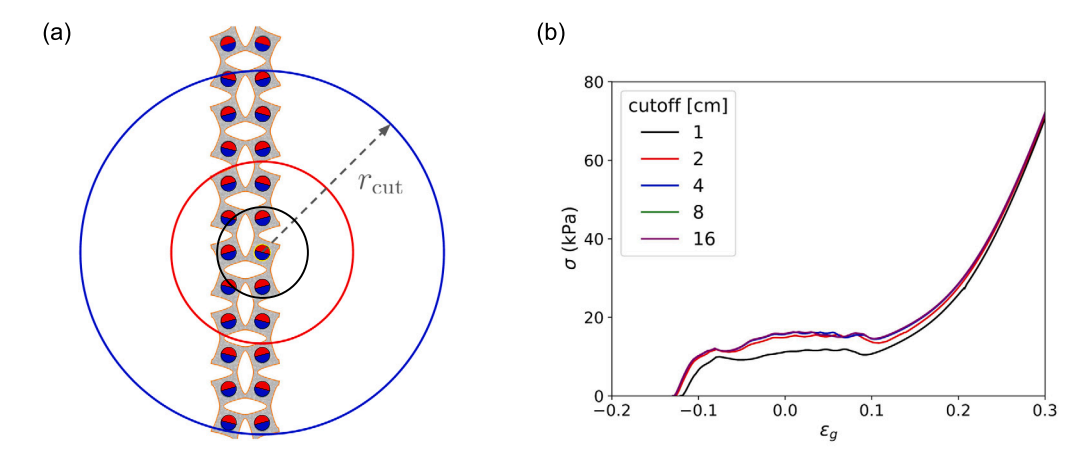


Fig. 10. Tensile test for Q = 1 using various cutoffs. (a) A schematic showing the range of some of the cutoffs used in (b) the stress–strain curves. The difference between $d_{\text{cut}} = 2$ cm and $d_{\text{cut}} = 4$ cm for this particular system is marginal.

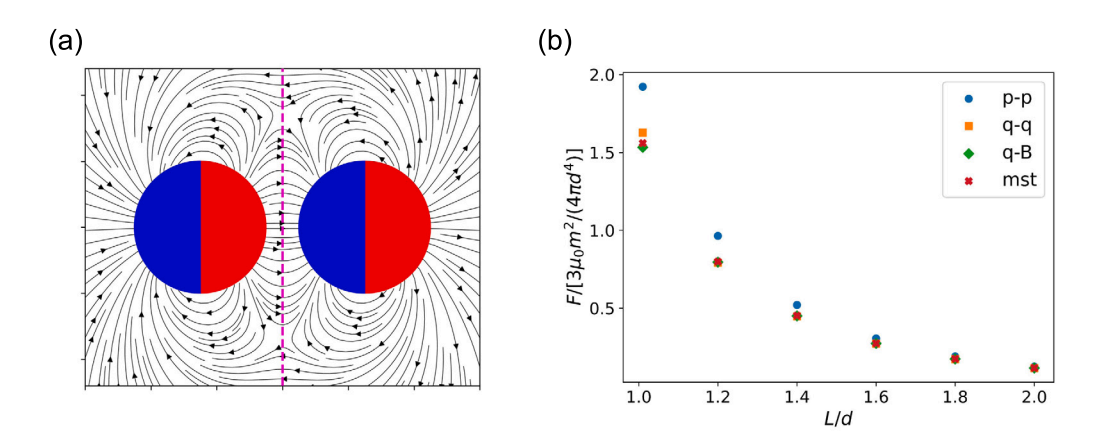


Fig. 11. (a) The magnetic field lines produced by two cylindrical magnets with uniform transverse magnetization in a particular configuration. The dashed line represents the midplane where the magnetic field is only in the normal direction. (b) Comparison of different methods to compute the force between the magnets: (p-p) point-dipole approximation, (q-q) fictitious charges interacting via Coulomb's law, (q-B) force law for fictitious charges, (mst) Maxwell stress tensor. Only (p-p) is an approximation. The other three methods are exact, and their differences are due to discretization.

dipoles, each interacting with every dipole in the other collection. Alternatively, a fictitious magnetic charge model may be used (Appendix A). This is equivalent to the Green's function approach used by Seyedkanani and Akbarzadeh (2022) to compute the force and torque on the magnets to avoid a more expensive FEM computation. The advantage of this formulation in a particle-based model is that the 'numerical integration' of the force and torque is automatically obtained from the forces on the particles that make up the rigid magnet.

In Fig. 11, we calculate the force between two transverse-magnetized cylindrical magnets with d = h, separated by a distance L, configured as shown in (a). The force is calculated using four methods with increasing accuracy: (p-p) point-dipole approximation, (q-q) charges interacting via Coulomb's law, (q-B) force law for magnetic charge (Eq. (A.3)), (mst) Maxwell stress tensor. For (p-p), each magnet was treated as a single dipole. For (q-q) and (q-B), discrete charges were computed on the nodes of a triangular mesh of the cylindrical surface; (q-B) is more accurate because only one magnet is meshed and the force is calculated using the exact magnetic field produced by the other magnet, which we obtained using Magpylib (Ortner and Bandeira, 2020). In (mst), the exact field produced by the two magnets was obtained, and the Maxwell stress tensor was numerically integrated over the midplane. Fig. 11(b) shows the force as a function of L. At L = 1.1d, the force obtained using the dipole approximation (p-p) is around 25% larger than the other methods; and this is only for the specific configuration shown in (a), the errors can be as large as 100% in general (Masiero and Sinibaldi, 2023; Petruska and Abbott, 2013).

The methods discussed here can be used to improve the accuracy of the magnetic behavior in the simulations when the singledipole approximation is insufficient. In LAMMPS, the discrete dipole or charge model may be the most straightforward to implement, and the computations can be accelerated by various long-range solvers.

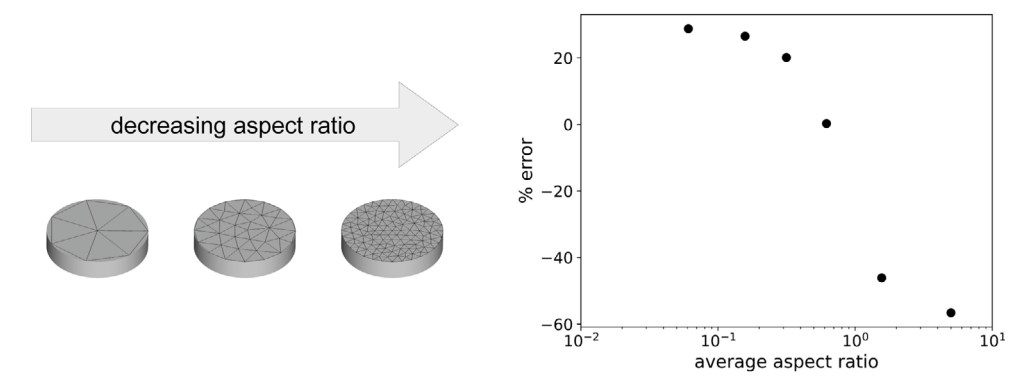


Fig. 12. The thickness of the magnet is important. Here, a disk magnet is discretized into dipoles. In 2D, a mesh refinement will only affect the cross-section, which will decrease the average aspect ratio of the dipole elements. The plot shows the error obtained in the force using the setup of Fig. 11 when L = 1.1d.

4.2. Distributed dipoles and aspect ratio

In the current work, we have treated each magnet as a 3D point-dipole. The simplified model is a reasonably good approximation if the magnet's shape is close to a sphere because the dipole model is exact for spheres (Hu, 2000; Edwards et al., 2017). If the thickness of the magnet is smaller than its in-plane dimensions, another strategy of improving the accuracy is to discretize the magnet into smaller dipoles. However, special attention should be paid to the shape of the small dipoles. We illustrate this by computing the force between two disk magnets in the setup in Fig. 11 at a center-to-center distance L = 1.1d using different discretized dipoles (shown in Fig. 12). Here, the aspect ratio of each cylinder is d/h = 5. We discretize the magnets' cross section with varying fineness and calculate the relative error, measured with respect to the value obtained using the (q-B) model, as a function of the average aspect ratio ($\sqrt{\text{area}}/h$) of the (triangular prism) mesh elements in Fig. 12. Assuming the magnet has a dipole moment m, we assigned at the center of each mesh element a dipole moment of ma/A, where a is the area of the element and $A = \pi d^2/4$. We can see that a finer mesh of discrete dipoles will not always give more accurate results. For the particular error measure we defined, the aspect ratio of ≈ 0.6 minimizes the error. A more rigorous measure will need an integral of errors at different points in the 3D space. Although the optimum ratio may change with different evaluation methods, the key message of the aspect ratio effect remains the same.

Petruska and Abbott (2013) found that the optimal aspect ratio for a cylinder is $d/h = \sqrt{4/3}$. For this geometry, the quadrupole moment vanishes. Finding the optimal aspect ratio for irregular shapes will be much more complicated, but this value can serve as a rough guide in choosing the proper dipole discretization. For example, cylindrical magnets with $d/h \approx 0.97$ were used in Section 3.4. Discretizing the magnet will only lower the average aspect ratio, deviating more from the optimum value. Therefore, the single-dipole approximation we started with is already the most accurate under the 2D assumption.

If the thickness is larger than the in-plane dimension, the magnet cannot be modeled accurately as a collection of co-planar dipoles, especially at close range since even the single-dipole approximation fails (i.e., the multipole expansion does not converge at distances less than h). For example, the cylindrical magnets in Section 3.3 have an aspect ratio of 1/6, so the single-dipole approximation will vastly overestimate the repulsive force. For these kinds of structures, it is better to use a 3D model with distributed dipoles along the thickness.

4.3. Lattice models and extension to 3D

One limitation of the triangular lattice spring model is that Poisson's ratio must be v = 1/3 (Seung and Nelson, 1988; Lloyd et al., 2007; Leembruggen et al., 2023). Moreover, the springs are permanent (i.e., no fracture) and harmonic, so they are only accurate for small-strain linear-elastic behavior. Some metamaterials rely on hyperelastic and viscoelastic response, which the current model cannot capture. The use of other lattice modeling schemes for hyperelastic material (Buxton et al., 2005; Zhang, 2019) can be explored in the future. Extending the current model to accommodate 3D structures will also open up new avenues for exploration and discovery. For shell structures, dihedral angles can be introduced to account for the bending energy in the LSM (Seung and Nelson, 1988; Leembruggen et al., 2023). For 3D structures, lattice spring models have been developed and implemented in LAMMPS for hard-magnetic soft composites (Ye et al., 2021; Jiang et al., 2023). In addition, the computer graphics community has used LSMs extensively and developed various algorithms (Terzopoulos et al., 1987; Liu et al., 2013; Baraff and Witkin, 2023), which can be potentially integrated in the current simulation framework.

For the magnetic interactions in 3D, the magnet can be discretized using a volume mesh and modeled as a collection of nodal dipoles. As discussed in the previous section, it is important to make the volume mesh elements close to, say, a cube or a perfect tetrahedron to improve the accuracy. It is also possible to use a surface mesh with the fictitious magnetic charge model. After the magnets are converted into effective dipoles or charges, they can be directly included in the LAMMPS simulations.

5. Conclusion

We have presented a simple framework for simulating planar mechanical structures with rigid inclusions of permanent magnets using the open-source LAMMPS MD software to address the need for modeling and simulation tools for the growing field of magneto-mechanical smart materials. This framework can be used to study how external magnetic field actuation and internal magnetic interactions couple with elastic deformations. We have demonstrated its versatility by showcasing a few representative simulations, including bistable configurations of an elastic beam with two magnets, magnetically tailored mechanical responses in lattice metamaterials with shape-locking effect, buckling of a soft cellular solid driven by a non-uniform magnetic field, and phase-transforming behaviors in metamaterial chains due to long-range magnetic interactions. Our simulations agree reasonably well with the previously reported experiments, validating the models. We also discuss the potential directions to further improve the accuracy and capabilities of the model.

Our framework is simple, versatile, and ready to use by harnessing the open-source framework. We envision that it can help supplement or guide analytical or empirical models, like those in Yasuda et al. (2020), Korpas et al. (2021), Liang et al. (2022), Liang and Crosby (2022), Jiao et al. (2024), which are tailored to the specific geometry and may not be easily generalized to more complicated unit cells. Our structure-agnostic model avoids the need to consider torsional and shear springs at the expense of adding more nodes. As another example, Yang et al. (2019) developed a theoretical framework to predict the auxetic behavior for various patterns of hard particles in a soft matrix. It would be interesting to explore the case where the hard particles are magnetic. The parallelization of LAMMPS can also enable us to simulate swarms to investigate collective behavior of these active structures (Gu et al., 2019, 2023; Yang et al., 2023; Yang and Keten, 2023). We also hope to extend our framework to accommodate deformable magnets in the future by incorporating the effect of deformation on the calculation of the effective dipoles or charges.

CRediT authorship contribution statement

Gabriel Alkuino: Writing – review & editing, Writing – original draft, Visualization, Software, Methodology, Data curation, Conceptualization. **Teng Zhang:** Writing – review & editing, Supervision, Methodology, Funding acquisition, Conceptualization.

Declaration of competing interest

The authors declare that they have no known competing financial interests or personal relationships that could have appeared to influence the work reported in this paper.

Data availability

The simulation codes and files are available at https://github.com/gsalkuin/lammps-magneto-mechanical-2d.

Declaration of Generative AI and AI-assisted technologies in the writing process

During the preparation of this work, the authors used ChatGPT to correct the grammar and enhance the flow of a few sentences. After using this tool/service, the authors reviewed and edited the content as needed and take full responsibility for the content of the publication.

Acknowledgments

The research was supported by the National Science Foundation, United States under Grant No. NSF CMMI-1847149 and NSF CMMI-2020476. Simulations were performed at the Expanse cluster (Award No. TG-PHY240004) in the Advanced Cyberinfrastructure Coordination Ecosystem: Services & Support (ACCESS) and the Zest high-performance computing cluster at Syracuse University. The authors would also like to acknowledge the anonymous reviewer for pointing out an important paper to strengthen our work.

Appendix A. Fictitious magnetic charges

In general, a magnetized body can be discretized into small dipole elements. However, in some cases this may not be the most practical model, especially if the magnetization is constant. In this case, we may adopt the fictitious magnetic charge model (Zangwill, 2013; Kremers et al., 2013; Van Dam et al., 2016; Caciagli et al., 2018; Ortner and Bandeira, 2020; Masiero and Sinibaldi, 2023). A modern treatment of the charge model can be found in Zangwill (2013), and we shall briefly summarize the relevant ideas. Assuming no free currents, for an isolated magnetized body with magnetization M(x), the net force due to an external field B_0 is

$$\mathbf{f} = \int_{\Omega} d\mathbf{f} = \int_{\Omega} (\mathbf{M}(\mathbf{x}) \cdot \nabla) \, \mathbf{B}_0(\mathbf{x}) \, dV. \tag{A.1}$$

Using the divergence theorem,

$$\int_{\partial \Omega} \mathbf{B}_0(\mathbf{M} \cdot \mathbf{n}) \, \mathrm{d}S = \int_{\Omega} \nabla \cdot (\mathbf{B}_0 \otimes \mathbf{M}) \, \mathrm{d}V = \int_{\Omega} \left[(\mathbf{M} \cdot \nabla) \mathbf{B}_0 + \mathbf{B}_0 (\nabla \cdot \mathbf{M}) \right] \, \mathrm{d}V \tag{A.2}$$

By defining a surface charge density $\sigma^* = \mathbf{M} \cdot \mathbf{n}$ and volume charge density $\rho^* = -\nabla \cdot \mathbf{M}$, we get the force law

$$\mathbf{f} = \int_{\partial\Omega} \sigma^*(\mathbf{x}) \mathbf{B}_0(\mathbf{x}) \, \mathrm{d}S + \int_{\Omega} \rho^*(\mathbf{x}) \mathbf{B}_0(\mathbf{x}) \, \mathrm{d}V. \tag{A.3}$$

Note that $\mathbf{B}_0(\mathbf{x})$ is the external magnetic field before the introduction of the body, which is generally the known quantity in magnetic actuation experiments. In this case, we can replace the external field as that produced by the other magnetic charges; i.e., the system reduces to an equivalent electrostatic system interacting via Coulomb's law. In a typical continuum approach, one first solves the total field $\mathbf{B}(\mathbf{x})$ upon introducing the body and then computes the force and torque from the Maxwell stress tensor. In this case, an extra surface term appears, analogous to the electrostatic pressure on conductors (Zangwill, 2013; Dorfmann and Ogden, 2014). To account for the relative permeability of the magnet, a correction factor can be added to the charges (Kremers et al., 2013).

Similarly, using the following identity

$$\int_{\partial\Omega} \mathbf{x} \times \mathbf{B}_{0}(\mathbf{M} \cdot \mathbf{n}) \, \mathrm{d}S = \int_{\Omega} \nabla \cdot (\mathbf{x} \times \mathbf{B}_{0} \otimes \mathbf{M}) \, \mathrm{d}V$$

$$= \int_{\Omega} \left[\mathbf{M} \times \mathbf{B}_{0} + \mathbf{x} \times (\mathbf{M} \cdot \nabla) \mathbf{B}_{0} + \mathbf{x} \times \mathbf{B}_{0}(\nabla \cdot \mathbf{M}) \right] \, \mathrm{d}V$$
(A.4)

the net torque, which is the sum of the body torque and force contributions, is given by

$$\mathbf{t} = \int_{V} \mathbf{M}(\mathbf{x}) \times \mathbf{B}_{0}(\mathbf{x}) \, dV + \int_{V} \mathbf{x} \times (\mathbf{M}(\mathbf{x}) \cdot \nabla) \, \mathbf{B}_{0}(\mathbf{x}) \, dV$$

$$= \int_{\partial O} \mathbf{x} \times \sigma^{*}(\mathbf{x}) \mathbf{B}_{0}(\mathbf{x}) \, dS + \int_{O} \mathbf{x} \times \rho^{*}(\mathbf{x}) \mathbf{B}_{0}(\mathbf{x}) \, dV. \tag{A.5}$$

For uniformly magnetized rigid magnets,² the fictitious magnetic charge model removes the rotational degree of freedom and, therefore, the need to compute gradients and torques. In addition, the magnetic charges only exist at surfaces, leading to fewer discrete point charges than dipoles in 3D structures, which is very promising in future modeling and simulations of 3D magneto-mechanical metamaterials.

Appendix B. Supplementary data

Supplementary material related to this article can be found online at https://doi.org/10.1016/j.jmps.2024.105759.

References

Abbasi, A., Chen, T., Aymon, B.F., Reis, P.M., 2024. Leveraging the snap buckling of bistable magnetic shells to design a refreshable braille dot. Adv. Mater. Technol. 9 (3), 2301344. http://dx.doi.org/10.1002/admt.202301344.

Arora, N., Chen, V., Cherkasov, A., Xiang, Y., Juhl, A., Buskohl, P., Rudykh, S., 2024. Magnetically-programmed instability-driven pattern transformations in soft materials. Adv. Funct. Mater. 2401077. http://dx.doi.org/10.1002/adfm.202401077.

Baraff, D., Witkin, A., 2023. Large steps in cloth simulation. In: Seminal Graphics Papers: Pushing the Boundaries, vol. 2, pp. 767–778. http://dx.doi.org/10. 1145/280814.280821.

Boncheva, M., Andreev, S.A., Mahadevan, L., Winkleman, A., Reichman, D.R., Prentiss, M.G., Whitesides, S., Whitesides, G.M., 2005. Magnetic self-assembly of three-dimensional surfaces from planar sheets. Proc. Natl. Acad. Sci. 102 (11), 3924–3929. http://dx.doi.org/10.1073/pnas.0500807102.

Borcea, L., Bruno, O., 2001. On the magneto-elastic properties of elastomer–ferromagnet composites. J. Mech. Phys. Solids 49 (12), 2877–2919. http://dx.doi.org/10.1016/S0022-5096(01)00108-9.

Brownstein, K., 1987. Unique shape of uniformly polarizable dielectrics. J. Math. Phys. 28 (4), 978-980. http://dx.doi.org/10.1063/1.527590.

Buxton, G.A., Verberg, R., Jasnow, D., Balazs, A.C., 2005. Newtonian fluid meets an elastic solid: Coupling lattice Boltzmann and lattice-spring models. Phys. Rev. E 71 (5), 056707. http://dx.doi.org/10.1103/PhysRevE.71.056707.

Caciagli, A., Baars, R.J., Philipse, A.P., Kuipers, B.W., 2018. Exact expression for the magnetic field of a finite cylinder with arbitrary uniform magnetization. J. Magn. Magn. Mater. 456, 423–432. http://dx.doi.org/10.1016/j.jmmm.2018.02.003.

Callaghan, E.E., 1960. The Magnetic Field of a Finite Solenoid, vol. 465, National Aeronautics and Space Administration.

Camacho, J.M., Sosa, V., 2013. Alternative method to calculate the magnetic field of permanent magnets with azimuthal symmetry. Rev. Mex. De Fís. E 59 (1), 8–17.

Castañeda, P.P., Galipeau, E., 2011. Homogenization-based constitutive models for magnetorheological elastomers at finite strain. J. Mech. Phys. Solids 59 (2), 194–215. http://dx.doi.org/10.1016/j.imps.2010.11.004.

Chen, Z., Kong, S., He, Y., Chen, S., Wang, W., Jin, L., Zhang, S., Hong, Y., Pan, L., Wu, H., et al., 2024. A magnet-driven soft bistable actuator. Adv. Funct. Mater. 2311498. http://dx.doi.org/10.1002/adfm.202311498.

Chen, T., Pauly, M., Reis, P.M., 2021. A reprogrammable mechanical metamaterial with stable memory. Nature 589 (7842), 386–390. http://dx.doi.org/10.1038/s41586-020-03123-5.

Danas, K., Kankanala, S., Triantafyllidis, N., 2012. Experiments and modeling of iron-particle-filled magnetorheological elastomers. J. Mech. Phys. Solids 60 (1), 120–138. http://dx.doi.org/10.1016/j.jmps.2011.09.006.

Danas, K., Reis, P.M., 2024. Stretch-independent magnetization in incompressible isotropic hard magnetorheological elastomers. J. Mech. Phys. Solids 191, 105764. http://dx.doi.org/10.1016/j.jmps.2024.105764.

Deng, H., Sattari, K., Xie, Y., Liao, P., Yan, Z., Lin, J., 2020. Laser reprogramming magnetic anisotropy in soft composites for reconfigurable 3D shaping. Nat. Commun. 11 (1), 6325. http://dx.doi.org/10.1038/s41467-020-20229-6.

² Note that only an ellipsoid can truly be uniformly magnetized (Brownstein, 1987), so for other shapes this is just an approximation.

- Deussen, O., Kobbelt, L., Tücke, P., 1995. Using simulated annealing to obtain good nodal approximations of deformable bodies. In: Terzopoulos, D., Thalmann, D. (Eds.), Computer Animation and Simulation '95. Springer Vienna, Vienna, pp. 30–43. http://dx.doi.org/10.1007/978-3-7091-9435-5_3, Series Title: Eurographics
- Dong, Y., Wang, L., Xia, N., Yang, Z., Zhang, C., Pan, C., Jin, D., Zhang, J., Majidi, C., Zhang, L., 2022. Untethered small-scale magnetic soft robot with programmable magnetization and integrated multifunctional modules. Sci. Adv. 8 (25), eabn8932. http://dx.doi.org/10.1126/sciadv.abn8932.
- Dorfmann, A., Ogden, R., 2003. Magnetoelastic modelling of elastomers. Eur. J. Mech. A Solids 22 (4), 497–507. http://dx.doi.org/10.1016/S0997-7538(03)00067-6
- Dorfmann, A., Ogden, R., 2004. Nonlinear magnetoelastic deformations of elastomers. Acta Mech. 167, 13–28. http://dx.doi.org/10.1007/s00707-003-0061-2. Dorfmann, L., Ogden, R.W., 2014. Nonlinear Theory of Electroelastic and Magnetoelastic Interactions, vol. 1, Springer, http://dx.doi.org/10.1007/978-1-4614-9596-3
- Edwards, B.F., Riffe, D.M., Ji, J.Y., Booth, W.A., 2017. Interactions between uniformly magnetized spheres. Am. J. Phys. 85 (2), 130–134. http://dx.doi.org/10. 1119/1.4973409.
- Galea, R., Dudek, K.K., Farrugia, P.-S., Zammit Mangion, L., Grima, J.N., Gatt, R., 2022. Reconfigurable magneto-mechanical metamaterials guided by magnetic fields. Compos. Struct. 280, 114921. http://dx.doi.org/10.1016/j.compstruct.2021.114921.
- Galipeau, E., Castañeda, P.P., 2013. A finite-strain constitutive model for magnetorheological elastomers: magnetic torques and fiber rotations. J. Mech. Phys. Solids 61 (4), 1065–1090. http://dx.doi.org/10.1016/j.jmps.2012.11.007.
- Garcia-Gonzalez, D., 2019. Magneto-visco-hyperelasticity for hard-magnetic soft materials: theory and numerical applications. Smart Mater. Struct. 28 (8), 085020. http://dx.doi.org/10.1088/1361-665X/ab2b05.
- Garcia-Gonzalez, D., Hossain, M., 2021a. A microstructural-based approach to model magneto-viscoelastic materials at finite strains. Int. J. Solids Struct. 208, 119–132. http://dx.doi.org/10.1016/j.ijsolstr.2020.10.028.
- Garcia-Gonzalez, D., Hossain, M., 2021b. Microstructural modelling of hard-magnetic soft materials: Dipole-dipole interactions versus Zeeman effect. Extreme Mech. Lett. 48, 101382. http://dx.doi.org/10.1016/j.eml.2021.101382.
- George, A., Mondal, S., Purnaprajna, M., Athri, P., 2022. Review of electrostatic force calculation methods and their acceleration in molecular dynamics packages using graphics processors. ACS Omega 7 (37), 32877–32896. http://dx.doi.org/10.1021/acsomega.2c03189.
- Geuzaine, C., Remacle, J.F., 2009. Gmsh: A 3-D finite element mesh generator with built-in pre- and post-processing facilities. Internat. J. Numer. Methods Engrg. 79 (11), 1309–1331. http://dx.doi.org/10.1002/nme.2579.
- Ginder, J.M., Nichols, M.E., Elie, L.D., Tardiff, J.L., 1999. Magnetorheological elastomers: Properties and applications. In: Smart Structures and Materials 1999: Smart Materials Technologies, vol. 3675, SPIE, pp. 131–138. http://dx.doi.org/10.1117/12.352787.
- Gu, H., Boehler, Q., Ahmed, D., Nelson, B.J., 2019. Magnetic quadrupole assemblies with arbitrary shapes and magnetizations. Science Robotics 4 (35), eaax8977. http://dx.doi.org/10.1126/scirobotics.aax8977.
- Gu, H., Möckli, M., Ehmke, C., Kim, M., Wieland, M., Moser, S., Bechinger, C., Boehler, Q., Nelson, B.J., 2023. Self-folding soft-robotic chains with reconfigurable shapes and functionalities. Nature Commun. 14 (1), 1263. http://dx.doi.org/10.1038/s41467-023-36819-z.
- Hu, B.Y.K., 2000. Averages of static electric and magnetic fields over a spherical region: A derivation based on the mean-value theorem. Am. J. Phys. 68 (11), 1058–1060. http://dx.doi.org/10.1119/1.1287349.
- Hu, W., Lum, G.Z., Mastrangeli, M., Sitti, M., 2018. Small-scale soft-bodied robot with multimodal locomotion. Nature 554 (7690), 81–85. http://dx.doi.org/10.1038/nature25443.
- Huang, W., Liu, M., Hsia, K.J., 2023. A discrete model for the geometrically nonlinear mechanics of hard-magnetic slender structures. Extreme Mech. Lett. 59, 101977. http://dx.doi.org/10.1016/j.eml.2023.101977.
- in 't Veld, P.J., Plimpton, S.J., Grest, G.S., 2008. Accurate and efficient methods for modeling colloidal mixtures in an explicit solvent using molecular dynamics. Comput. Phys. Commut. 179, 320–329. http://dx.doi.org/10.1016/j.cpc.2008.03.005.
- Jacobson, A., Panozzo, D., et al., 2018. libigl: A simple C++ geometry processing library. https://libigl.github.io/.
- Jiang, H., Gu, H., Nelson, B.J., Zhang, T., 2023. Numerical study of metachronal wave-modulated locomotion in magnetic cilia carpets. Adv. Intell. Syst. 5 (10), 2300212. http://dx.doi.org/10.1002/aisy.202300212.
- Jiao, W., Shu, H., Tournat, V., Yasuda, H., Raney, J.R., 2024. Phase transitions in 2D multistable mechanical metamaterials via collisions of soliton-like pulses. Nature Commun. 15 (1), 333. http://dx.doi.org/10.1038/s41467-023-44293-w.
- Jolly, M.R., Carlson, J.D., Muñoz, B.C., 1996. A model of the behaviour of magnetorheological materials. Smart Mater. Struct. 5 (5), 607–614. http://dx.doi.org/10.1088/0964-1726/5/5/009.
- Kim, Y., Yuk, H., Zhao, R., Chester, S.A., Zhao, X., 2018. Printing ferromagnetic domains for untethered fast-transforming soft materials. Nature 558 (7709), 274–279. http://dx.doi.org/10.1038/s41586-018-0185-0.
- Kim, Y., Zhao, X., 2022. Magnetic soft materials and robots. Chem. Rev. 122 (5), 5317-5364. http://dx.doi.org/10.1021/acs.chemrev.1c00481.
- Korpas, L.M., Yin, R., Yasuda, H., Raney, J.R., 2021. Temperature-responsive multistable metamaterials. ACS Appl. Mater. Interfaces 13 (26), 31163–31170. http://dx.doi.org/10.1021/acsami.1c07327.
- Kremers, M.F., Paulides, J.J., Ilhan, E., Janssen, J.L., Lomonova, E.A., 2013. Relative permeability in a 3D analytical surface charge model of permanent magnets. IEEE Trans. Magn. 49 (5), 2299–2302. http://dx.doi.org/10.1109/TMAG.2013.2239976.
- Leembruggen, M., Andrejevic, J., Kudrolli, A., Rycroft, C.H., 2023. Computational model of twisted elastic ribbons. Phys. Rev. E 108 (1), 015003. http://dx.doi.org/10.1103/PhysRevE.108.015003.
- Li, J., Barjuei, E.S., Ciuti, G., Hao, Y., Zhang, P., Menciassi, A., Huang, Q., Dario, P., 2018. Magnetically-driven medical robots: An analytical magnetic model for endoscopic capsules design. J. Magn. Magn. Mater. 452, 278–287. http://dx.doi.org/10.1016/j.jmmm.2017.12.085.
- Li, L., Yao, H., Mi, S., 2023. Magnetically driven modular mechanical metamaterials with high programmability, reconfigurability, and multiple applications. ACS Appl. Mater. Interfaces 15 (2), 3486–3496. http://dx.doi.org/10.1021/acsami.2c19679, Publisher: American Chemical Society.
- Liang, X., Crosby, A.J., 2022. Dynamic recoil in metamaterials with nonlinear interactions. J. Mech. Phys. Solids 162, 104834. http://dx.doi.org/10.1016/j.jmps. 2022.104834.
- Liang, X., Fu, H., Crosby, A.J., 2022. Phase-transforming metamaterial with magnetic interactions. Proc. Natl. Acad. Sci. 119 (1), e2118161119. http://dx.doi.org/10.1073/pnas.2118161119, Publisher: Proceedings of the National Academy of Sciences.
- Liu, L., 2014. An energy formulation of continuum magneto-electro-elasticity with applications. J. Mech. Phys. Solids 63, 451–480. http://dx.doi.org/10.1016/j. imps.2013.08.001.
- Liu, T., Bargteil, A.W., O'Brien, J.F., Kavan, L., 2013. Fast simulation of mass-spring systems. ACM Trans. Graph. 32 (6), 1–7. http://dx.doi.org/10.1145/2508363. 2508406.
- Lloyd, B., Szekely, G., Harders, M., 2007. Identification of spring parameters for deformable object simulation. IEEE Trans. Vis. Comput. Graphics 13 (5), 1081–1094. http://dx.doi.org/10.1109/TVCG.2007.1055, Conference Name: IEEE Transactions on Visualization and Computer Graphics.
- Loukaides, E., Smoukov, S., Seffen, K., 2014. Magnetic actuation and transition shapes of a bistable spherical cap. Int. J. Smart Nano Mater. 5 (4), 270–282. http://dx.doi.org/10.1080/19475411.2014.997322.
- Lu, L., Sim, J., Zhao, R.R., 2023. Mechanics of hard-magnetic soft materials: A review. Mech. Mater. 104874. http://dx.doi.org/10.1016/j.mechmat.2023.104874.

- Mahmood, A.U., Yingling, Y.G., 2022. All-atom simulation method for Zeeman alignment and dipolar assembly of magnetic nanoparticles. J. Chem. Theory Comput. 18 (5), 3122–3135. http://dx.doi.org/10.1021/acs.jctc.1c01253, PMID: 35271259.
- Masiero, F., Sinibaldi, E., 2023. Exact and computationally robust solutions for cylindrical magnets systems with programmable magnetization. Adv. Sci. 10 (25), 2301033. http://dx.doi.org/10.1002/advs.202301033.
- Montgomery, S.M., Wu, S., Kuang, X., Armstrong, C.D., Zemelka, C., Ze, Q., Zhang, R., Zhao, R., Qi, H.J., 2021. Magneto-mechanical metamaterials with widely tunable mechanical properties and acoustic bandgaps. Adv. Funct. Mater. 31 (3), 2005319. http://dx.doi.org/10.1002/adfm.202005319.
- Monti, J.M., Clemmer, J.T., Srivastava, I., Silbert, L.E., Grest, G.S., Lechman, J.B., 2022. Large-scale frictionless jamming with power-law particle size distributions. Phys. Rev. E 106, http://dx.doi.org/10.1103/PhysRevE.106.034901.
- Mukherjee, D., Bodelot, L., Danas, K., 2020. Microstructurally-guided explicit continuum models for isotropic magnetorheological elastomers with iron particles. Int. J. Non-Linear Mech. 120, 103380. http://dx.doi.org/10.1016/j.ijnonlinmec.2019.103380.
- Mukherjee, D., Rambausek, M., Danas, K., 2021. An explicit dissipative model for isotropic hard magnetorheological elastomers. J. Mech. Phys. Solids 151, 104361. http://dx.doi.org/10.1016/j.jmps.2021.104361.
- Niu, R., Du, C.X., Esposito, E., Ng, J., Brenner, M.P., McEuen, P.L., Cohen, I., 2019. Magnetic handshake materials as a scale-invariant platform for programmed self-assembly. Proc. Natl. Acad. Sci. 116 (49), 24402–24407. http://dx.doi.org/10.1073/pnas.1910332116.
- Ortner, M., Bandeira, L.G.C., 2020. Magpylib: A free Python package for magnetic field computation. SoftwareX 11, 100466. http://dx.doi.org/10.1016/j.softx. 2020.100466.
- Ostoja-Starzewski, M., 2002. Lattice models in micromechanics. Appl. Mech. Rev. 55 (1), 35-60. http://dx.doi.org/10.1115/1.1432990.
- Pal, A., Sitti, M., 2023. Programmable mechanical devices through magnetically tunable bistable elements. Proc. Natl. Acad. Sci. 120 (15), e2212489120. http://dx.doi.org/10.1073/pnas.2212489120.
- Petruska, A.J., Abbott, J.J., 2013. Optimal permanent-magnet geometries for dipole field approximation. IEEE Trans. Magn. 49 (2), 811–819. http://dx.doi.org/10.1109/TMAG.2012.2205014.
- Pezzulla, M., Yan, D., Reis, P.M., 2022. A geometrically exact model for thin magneto-elastic shells. J. Mech. Phys. Solids 166, 104916. http://dx.doi.org/10.1016/j.jmps.2022.104916.
- Rambausek, M., Mukherjee, D., Danas, K., 2022. A computational framework for magnetically hard and soft viscoelastic magnetorheological elastomers. Comput. Methods Appl. Mech. Engrg. 391, 114500. http://dx.doi.org/10.1016/j.cma.2021.114500.
- Sano, T.G., 2022. Reduced theory for hard magnetic rods with dipole-dipole interactions. J. Phys. A 55 (10), 104002. http://dx.doi.org/10.1088/1751-8121/ac4de2.
- Sano, T.G., Pezzulla, M., Reis, P.M., 2022. A Kirchhoff-like theory for hard magnetic rods under geometrically nonlinear deformation in three dimensions. J. Mech. Phys. Solids 160, 104739. http://dx.doi.org/10.1016/j.jmps.2021.104739.
- Schlömer, N., nilswagner, Li, T., Coutinho, C., Dalcin, L., McBain, G., Cervone, A., Langlois, T., Peak, S., Bussonnier, M., Igiraldi, Vaillant, G.A., Croucher, A., 2018. Nschloe/meshio v1.11.7. http://dx.doi.org/10.5281/zenodo.1173116.
- Seung, H.S., Nelson, D.R., 1988. Defects in flexible membranes with crystalline order. Phys. Rev. A 38 (2), 1005–1018. http://dx.doi.org/10.1103/PhysRevA.38.
- Seyedkanani, A., Akbarzadeh, A., 2022. Magnetically assisted rotationally multistable metamaterials for tunable energy trapping-dissipation. Adv. Funct. Mater. 32 (52), 2207581. http://dx.doi.org/10.1002/adfm.202207581.
- Shire, T., Hanley, K.J., Stratford, K., 2020. DEM simulations of polydisperse media: Efficient contact detection applied to investigate the quasi-static limit. Comput. Part. Mech. http://dx.doi.org/10.1007/s40571-020-00361-2.
- Sim, J., Wu, S., Dai, J., Zhao, R.R., 2023. Magneto-mechanical bilayer metamaterial with global area-preserving density tunability for acoustic wave regulation. Adv. Mater. 35 (35), 2303541. http://dx.doi.org/10.1002/adma.202303541.
- Slesarenko, V., 2020. Planar mechanical metamaterials with embedded permanent magnets. Materials 13 (6), 1313. http://dx.doi.org/10.3390/ma13061313.
- Steiner, J.A., Pham, L.N., Abbott, J.J., Leang, K.K., 2022. Modeling and analysis of a soft endoluminal inchworm robot propelled by a rotating magnetic dipole field. J. Mech. Robot. 14 (5), 051002. http://dx.doi.org/10.1115/1.4053114.
- Stewart, E.M., Anand, L., 2023. Magneto-viscoelasticity of hard-magnetic soft-elastomers: Application to modeling the dynamic snap-through behavior of a bistable arch. J. Mech. Phys. Solids 179, 105366. http://dx.doi.org/10.1016/j.jmps.2023.105366.
- Stukowski, A., 2010. Visualization and analysis of atomistic simulation data with OVITO-the open visualization tool. Model. Simul. Mater. Sci. Eng. 18 (1), http://dx.doi.org/10.1088/0965-0393/18/1/015012.
- Surjadi, J.U., Gao, L., Du, H., Li, X., Xiong, X., Fang, N.X., Lu, Y., 2019. Mechanical metamaterials and their engineering applications. Adv. Eng. Mater. 21 (3), 1800864. http://dx.doi.org/10.1002/adem.201800864.
- Terzopoulos, D., Platt, J., Barr, A., Fleischer, K., 1987. Elastically deformable models. ACM SIGGRAPH Comput. Graph. 21 (4), 205–214. http://dx.doi.org/10. 1145/37402.37427.
- Thompson, A.P., Aktulga, H.M., Berger, R., Bolintineanu, D.S., Brown, W.M., Crozier, P.S., In't Veld, P.J., Kohlmeyer, A., Moore, S.G., Nguyen, T.D., et al., 2022. LAMMPS-A flexible simulation tool for particle-based materials modeling at the atomic, meso, and continuum scales. Comput. Phys. Comm. 271, 108171. http://dx.doi.org/10.1016/j.cpc.2021.108171.
- Tipton, C., Han, E., Mullin, T., 2012. Magneto-elastic buckling of a soft cellular solid. Soft Matter 8 (26), 6880–6883. http://dx.doi.org/10.1039/C2SM25965F. Tiryaki, M.E., Elmacioğlu, Y.G., Sitti, M., 2023. Magnetic guidewire steering at ultrahigh magnetic fields. Sci. Adv. 9 (17), eadg6438. http://dx.doi.org/10.1126/sciadv.adg6438.
- Van Dam, J., Paulides, J., Robertson, W.S., Dhaens, M., Lomonova, E., 2016. Analytical surface charge method for rotated permanent magnets: Boundary element method comparison and experimental validation. IEEE Trans. Magn. 52 (7), 1–4. http://dx.doi.org/10.1109/TMAG.2016.2517658.
- Vella, D., du Pontavice, E., Hall, C.L., Goriely, A., 2014. The magneto-elastica: From self-buckling to self-assembly. Proc. R. Soc. A: Math., Phys. Eng. Sci. 470 (2162), 20130609. http://dx.doi.org/10.1098/rspa.2013.0609.
- Wan, G., Avis, S.J., Wang, Z., Wang, X., Kusumaatmaja, H., Zhang, T., 2024. Finding transition state and minimum energy path of bistable elastic continua through energy landscape explorations. J. Mech. Phys. Solids 183, 105503. http://dx.doi.org/10.1016/j.jmps.2023.105503.
- Wang, L., Kim, Y., Guo, C.F., Zhao, X., 2020. Hard-magnetic elastica. J. Mech. Phys. Solids 142, 104045. http://dx.doi.org/10.1016/j.jmps.2020.104045.
- Wu, S., Eichenberger, J., Dai, J., Chang, Y., Ghalichechian, N., Zhao, R.R., 2022. Magnetically actuated reconfigurable metamaterials as conformal electromagnetic filters. Adv. Intell. Syst. 4 (9), 2200106. http://dx.doi.org/10.1002/aisy.202200106.
- Yan, D., Aymon, B.F., Reis, P.M., 2023. A reduced-order, rotation-based model for thin hard-magnetic plates. J. Mech. Phys. Solids 170, 105095. http://dx.doi.org/10.1016/j.jmps.2022.105095.
- Yan, D., Pezzulla, M., Cruveiller, L., Abbasi, A., Reis, P.M., 2021. Magneto-active elastic shells with tunable buckling strength. Nat. Commun. 12 (1), 2831. http://dx.doi.org/10.1038/s41467-021-22776-y.
- Yang, W., Gao, Z., Yue, Z., Li, X., Xu, B., 2019. Hard-particle rotation enabled soft–hard integrated auxetic mechanical metamaterials. Proc. R. Soc. A: Math., Phys. Eng. Sci. 475 (2228), 20190234. http://dx.doi.org/10.1098/rspa.2019.0234, Publisher: Royal Society.
- Yang, X., Keten, S., 2023. Emergent elasticity relations for networks of bars with sticky magnetic ends. Extreme Mech. Lett. 65, 102093. http://dx.doi.org/10.1016/j.eml.2023.102093.

- Yang, X., Leng, J., Sun, C., Keten, S., 2023. Self-assembled robust 2D networks from magneto-elastic bars. Adv. Mater. Technol. 2202189. http://dx.doi.org/10.1002/admt.202202189.
- Yasuda, H., Korpas, L., Raney, J., 2020. Transition waves and formation of domain walls in multistable mechanical metamaterials. Phys. Rev. Appl. 13 (5), 054067. http://dx.doi.org/10.1103/PhysRevApplied.13.054067.
- Ye, H., Li, Y., Zhang, T., 2021. Magttice: A lattice model for hard-magnetic soft materials. Soft Matter 17 (13), 3560–3568. http://dx.doi.org/10.1039/DOSM01662D.
- Yu, K., Fang, N.X., Huang, G., Wang, Q., 2018. Magnetoactive acoustic metamaterials. Adv. Mater. 30 (21), 1706348. http://dx.doi.org/10.1002/adma.201706348. Zangwill, A., 2013. Modern Electrodynamics. Cambridge University Press.
- Ze, Q., Kuang, X., Wu, S., Wong, J., Montgomery, S.M., Zhang, R., Kovitz, J.M., Yang, F., Qi, H.J., Zhao, R., 2020. Magnetic shape memory polymers with integrated multifunctional shape manipulation. Adv. Mater. 32 (4), 1906657. http://dx.doi.org/10.1002/adma.201906657.
- Zhang, T., 2019. Deriving a lattice model for neo-Hookean solids from finite element methods. Extreme Mech. Lett. 26, 40–45. http://dx.doi.org/10.1016/j.eml. 2018.11.007.
- Zhang, Q., Cherkasov, A.V., Arora, N., Hu, G., Rudykh, S., 2023a. Magnetic field-induced asymmetric mechanical metamaterials. Extreme Mech. Lett. 59, 101957. http://dx.doi.org/10.1016/j.eml.2023.101957.
- Zhang, Q., Cherkasov, A.V., Xie, C., Arora, N., Rudykh, S., 2023b. Nonlinear elastic vector solitons in hard-magnetic soft mechanical metamaterials. Int. J. Solids Struct. 280, 112396. http://dx.doi.org/10.1016/j.ijsolstr.2023.112396.
- Zhao, R., Kim, Y., Chester, S.A., Sharma, P., Zhao, X., 2019. Mechanics of hard-magnetic soft materials. J. Mech. Phys. Solids 124, 244–263. http://dx.doi.org/10.1016/j.jmps.2018.10.008.
- Zou, B., Liang, Z., Zhong, D., Cui, Z., Xiao, K., Shao, S., Ju, J., 2023. Magneto-thermomechanically reprogrammable mechanical metamaterials. Adv. Mater. 35 (8), 2207349. http://dx.doi.org/10.1002/adma.202207349.